Sound & Vibration 2025, 59(4), 3343.
doi: https://doi.org/10.59400/sv3343

Article

Why pile-soil interaction matters: dynamic characteristics and vibration suppression in large offshore wind turbines

Yang Xue[1], Linan Li[2,*], Jia Han[3], Huixin Wei[4,*], Shibin Wang[2], Haikun Jia[1], Lingxing Kong[1]

[1] China Electric Power Research Institute, Beijing 100192, China
[2] The School of Mechanical Engineering, Tianjin University, Tianjin 300354, China
[3] China State Shipbuilding Corporation Haizhuang Windpower Co., Ltd., Chongqing 400000, China
[4] The School of Infrastructure Engineering, Nanchang University, Nanchang 330031, China
*** Corresponding author:** Linan Li, lali@tju.edu.cn; Huixin Wei, hx_wei@ncu.edu.cn

CITATION

Xue Y, Li L, Han J, et al. Why pile-soil interaction matters: dynamic characteristics and vibration suppression in large offshore wind turbines. Sound & Vibration. 2025; 59(4): 3343. https://doi.org/10.59400/sv3343

ARTICLE INFO

Received: 6 June 2025
Revised: 16 August 2025
Accepted: 21 August 2025
Available online: 31 August 2025

Abstract: In the complex marine environment characterized by wind, waves and soils, the dynamic behavior of offshore wind turbines (OWTs) is highly intricate due to the coupled interactions among various components. However, current research often neglects soil-pile interaction. This study develops a dynamic analytical model of the entire OWT system incorporating soil-pile interaction based on the Euler-Lagrange equations. Wind, wave and soil loads are respectively calculated using blade element momentum theory, Morison's equation and $p-y$ curves. The dynamic responses of structural components, including blades, tower and monopile, under combined wind-wave-soil loads are then evaluated. A comparative analysis is conducted to examine the effects of soil-pile interaction and varying damping ratios on the frequency response of a 22-MW OWT. Results indicate that considering the monopile support structure and ignoring soil-pile interaction significantly underestimates the soil's contribution to structural stiffness and equivalent damping. For example, Fourier amplitude spectra curves reveal that soil-pile interaction shifts the dominant frequency and reduces peak displacements by over 30%. This refined methodology enables a more physically consistent representation of soil-pile interaction dynamics by explicitly incorporating the nonlinear behavior at the pile-soil interface. The enhanced framework effectively captures critical phenomena such as soil-induced frequency shifts and damping-mediated amplitude attenuation, which are essential for accurate resonance avoidance and fatigue life estimation in practical engineering applications.

Keywords: large-scale offshore wind turbine; pile-soil interaction; dynamic response; frequency shift; vibration suppression; 22-MW wind turbine

1. Introduction

Global energy consumption has surged dramatically, accompanied by sustained expansion in energy supply. As a pivotal cornerstone of the global renewable energy transition, wind power has experienced transformative advancements in recent years, characterized by rapid growth in installed capacity and technological innovation [1]. Optimizing wind resource efficiency is crucial for reducing carbon emissions and accelerating progress toward carbon neutrality targets [2].

Offshore wind power has entered into a competitive bidding era, with nearly all countries possessing offshore wind resources actively exploring deep-sea wind energy [3]. Turbines with higher capacity produce more electricity and provide greater

economic benefits. Consequently, large-scale offshore wind turbines (OWTs) have high practical value in reducing costs and improving efficiency [4, 5]. However, the upscaling of OWTs also brings increased structural dimensions and more complex loading conditions. On the one hand, tall OWTs lead to structural flexibility and become a critical factor that may lead to catastrophic failure. On the other hand, OWTs need to withstand complex marine conditions, including strong winds, waves, tides and soil conditions. These environmental factors necessitate stringent stability and safety criteria for foundation design.

The dynamic response of wind turbines involves coupled interactions among rotor blades, tower and supporting subsystems under combined environmental loads (wind/wave/soil) and operational blade rotation [6]. Researchers have investigated such dynamic behavior of wind turbines through theoretical analysis, experiments and numerical simulations, with the latter being the predominant methodology due to its flexibility. For instance, Bazeos et al. [7] developed a detailed finite element model of a 450-kW turbine using NISA software to analyze load-bearing and seismic behavior. With the increase of installed capacity, a self-developed simulation platform was then used to study the dynamic response of a 5-MW turbine under varying wind speeds and seismic intensities [8]. Sørum et al. [9] employed SIMA, vpOne and FAST to simulate the dynamic response of a bottom-fixed 10-MW OWT and assessed the fatigue life of its monopile at the mudline. For wind turbines in cold climates, Song et al. [10] simulated sea ice-wind load interactions via finite element method to assess dynamic responses. To investigate the dynamic behavior of a 15-MW OWT under wind-wave-current and seismic loads, a fully coupled numerical model was established to obtain the natural frequencies and structural responses [11]. However, despite their adaptability, numerical methods face unresolved challenges in multiphysics coupling of aerodynamic loads, exhibiting constrained computational scalability for full-system dynamic simulations.

In experimental investigations, Lu et al. [12] designed a 1:15 scale model of a 6.45-MW turbine to conduct shaking table tests to investigate seismic response. Zeng et al. [13] performed physical model tests with a 1:80 scale turbine to study the dynamic behavior under irregular wave loading. However, full-scale experimental validation remains technically and economically challenging due to prohibitive costs and methodological constraints. Theoretical advancements in dynamic response analysis of wind turbines have been achieved through refined analytical formulations and numerical frameworks. Sun et al. [14] proposed an analytical model of a monopile wind turbine to investigate vibration questions under wind and wave loads. Yang et al. [15] developed a fully coupled dynamic model for a 10-MW monopile offshore wind turbine, integrating wind, wave and seismic excitations. The effectiveness of a tuned mass damper under seismic loading was explored. Jahangiri et al. [16] developed a numerical model of a floating OWT, demonstrating that a damper could effectively suppress vibrations. However, existing research predominantly characterizes the dynamic response of wind turbines under combined wind-wave-earthquake loading, yet overlooks the soil-foundation interaction effect [17].

Complex environmental loads, such as wind and waves, are ultimately transmitted

to the foundation as bending moments and torques. The selection of OWT foundations is governed by multiple engineering parameters, notably water depth, seabed geotechnical properties, turbine capacity and structural design requirements. Monopile foundations are the most widely used globally. Soil-pile interaction (SPI) is inherently characterized by dynamic behaviors dependent on external loading and exhibits significant nonlinearity.

Oversimplified assumptions, which treat the soil-pile system as a rigid boundary constraint or employ constant-stiffness matrix formulations, fail to characterize the actual dynamic characteristics of OWT. It is thus of critical importance to accurately incorporate the time-varying SPI effect into the dynamic behaviors of OWT. Several studies have attempted to address this issue. Prowell et al. [18] developed a detailed 3D model of a 5-MW wind turbine using OpenSees, incorporating simplified blades, tower, nacelle and soil, to analyze soil-structure interaction. Abhinav et al. [19] used FAST to investigate the time-domain response and natural frequencies of a 5-MW turbine with soil effects. Wang et al. [20] developed a dynamic analysis method accounting for SPI effect to determine the impact of soil softening around the pile on lateral dynamic response. Akwaa and Gao [21] analyzed monopile dynamics using Abaqus by modeling the pile as a beam on an elastic foundation.

Soil-foundation interaction significantly affects the overall dynamic behavior of OWTs [22]. However, most existing models focus on separate modeling rather than considering the coupled interaction of wind, wave, blade rotation and soil loads. This study develops an analytical dynamic model of a monopile OWT using the Euler-Lagrange approach, incorporating time-varying soil-pile interaction. The model evaluates the dynamic response of a 22-MW OWT under combined wind-wave-soil-blade rotation loads and investigates the influence of pile-soil stiffness and damping on system dynamics.

2. Methods

2.1. Integrated model of OWT

Based on the deformation characteristics of each component of a monopile OWT under the combined action of wind, waves and soil, twelve degrees of freedom are defined across the blades, tower and pile structure, as illustrated in **Figure 1**. The origin of the global coordinate system is set at the intersection between the sea surface and the supporting structure. The parameters q_1, q_2, q_3, q_8, q_{10} and q_{12} represent the in-plane displacements of the blades, while the parameters q_4, q_5, q_6, q_7, q_9 and q_{11} are the out-of-plane displacements. Based on these definitions, the displacement, velocity and acceleration of each component can be determined.

Due to the rotation at the bottom of the pile is relatively small, the displacements u_{pile}^{x} and u_{pile}^{y} in the *x*- and *y*- directions of a differential element dz located the distance z above the pile tip can be approximated as

$$\begin{aligned} u_{pile}^{x} &= q_9 + z\tan q_{11} \approx q_9 + zq_{11} \\ u_{pile}^{y} &= q_{10} - z\tan q_{12} \approx q_{10} - zq_{12} \end{aligned}. \tag{1}$$

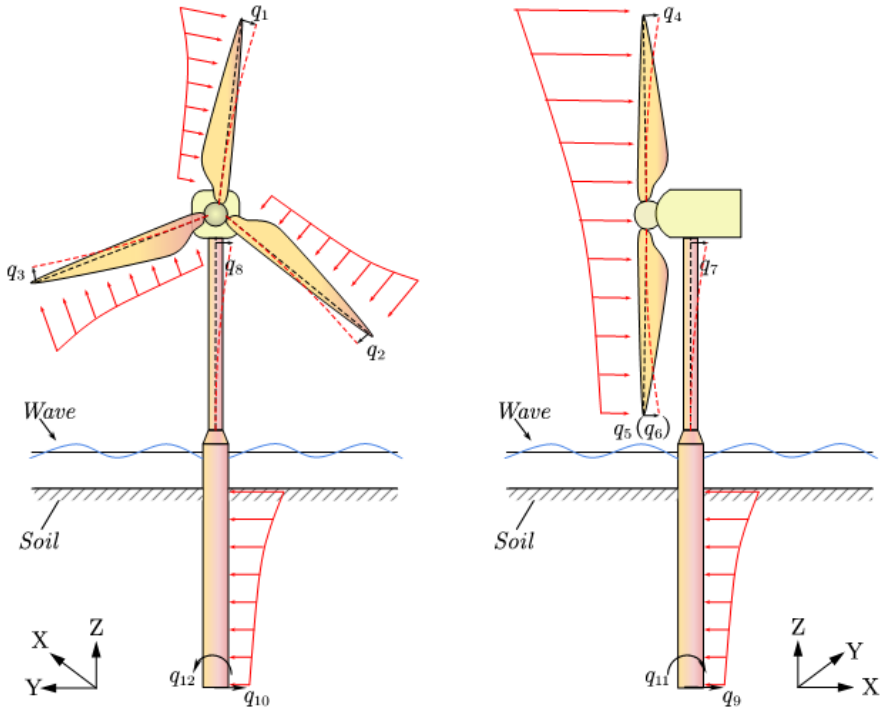

Figure 1. Model of the OWT structure.

The corresponding velocity components can be determined byss

$$\begin{aligned} \dot{u}_{pile}^{x} &\approx \dot{q}_9 + z\dot{q}_{11} \\ \dot{u}_{pile}^{y} &\approx \dot{q}_{10} - z\dot{q}_{12} \end{aligned}. \tag{2}$$

The absolute velocity of the pile at a distance z is expressed as

$$\dot{u}_{pile} = \sqrt{\left(\dot{u}_{pile}^{x}\right)^2 + \left(\dot{u}_{pile}^{y}\right)^2}. \tag{3}$$

Using a similar approach, the velocity components and the absolute velocity of the tower can be obtained by

$$\begin{aligned} \dot{u}_{tow}^{x} &\approx \varphi_{1x}\dot{q}_7 + \dot{q}_9 + z\dot{q}_{11} \\ \dot{u}_{tow}^{y} &\approx \varphi_{1y}\dot{q}_8 + \dot{q}_{10} - z\dot{q}_{12} \\ \dot{u}_{tow} &= \sqrt{\left(\dot{u}_{tow}^{x}\right)^2 + \left(\dot{u}_{tow}^{y}\right)^2} \end{aligned}, \tag{4}$$

where φ_{1x} and φ_{1y} are the first mode shape functions of tower deformation in the x and y-directions, respectively [16]. These are typically given as $\varphi_{1x} = \varphi_{1y} = -0.1154\overline{h}^6 + 0.1167\overline{h}^5 - 0.0908\overline{h}^4 + 0.2205\overline{h}^3 + 0.8689\overline{h}^2$, where $\overline{h}$ is the normalized height of the tower.

For simplification, the nacelle and hub are treated as a rigid body without additional deformation. Their velocity components can be approximated as

$$\begin{aligned} u_{nax}^{x} &\approx \dot{q}_7 + \dot{q}_9 + h_n\dot{q}_{11} \\ u_{nax}^{y} &\approx \dot{q}_8 + \dot{q}_{10} - h_n\dot{q}_{12} \\ \dot{u}_{nax} &= \sqrt{\left(\dot{u}_{nax}^{x}\right)^2 + \left(\dot{u}_{nax}^{y}\right)^2} \end{aligned}, \tag{5}$$

where h_n is the distance from the hub's center of mass to the pile tip.

Assuming the turbine blades rotate with angular velocity w, the rotational angle ϕ_j of the j-th blade is defined as

$$\phi_j = wt + \frac{2\pi}{3}(j-1), \quad j = 1,\ 2,\ 3. \tag{6}$$

The velocity components at a radial location dr on the j-th blade can then be described as

$$\begin{aligned} \dot{u}^x_{b,j}(r) &\approx \dot{q}_7 + \dot{q}_9 + h_n\dot{q}_{11} + \varphi_{2x}\dot{q}_{j+3} \\ \dot{u}^y_{b,j}(r) &\approx \dot{q}_8 + \dot{q}_{10} - h_n\dot{q}_{12} + wr\cos\phi_j \\ &\quad + \varphi_{2y}\dot{q}_j\cos\phi_j - w\varphi_{2y}q_j\sin\phi_j \\ \dot{u}^z_{b,j}(r) &= -wr\sin\phi_j - \varphi_{2y}\dot{q}_j\sin\phi_j - w\varphi_{2y}q_j\cos\phi_j \\ \dot{u}_{b,j} &= \sqrt{\left(\dot{u}^x_{b,j}\right)^2 + \left(\dot{u}^y_{b,j}\right)^2 + \left(\dot{u}^z_{b,j}\right)^2} \end{aligned}, \tag{7}$$

where φ_{2x} and φ_{2y} represent the mode shapes of blade deformation in the *x* and *y*-directions [16], respectively, and are given by

$$\begin{aligned} \varphi_{2x} &= -0.6952\overline{r}^6 + 2.3760\overline{r}^5 - 3.5772\overline{r}^4 + 2.5337\overline{r}^3 + 0.3627\overline{r}^2 \\ \varphi_{2y} &= -2.2555\overline{r}^6 + 4.7131\overline{r}^5 - 3.2452\overline{r}^4 + 1.7254\overline{r}^3 + 0.0622\overline{r}^2 \end{aligned}, \tag{8}$$

where $\overline{r}$ is the normalized length along the blade.

2.2. Dynamic equations

During the operation of the OWT, the blades rotate at a constant angular velocity. The total kinetic energy of the system essentially consists of the kinetic energy contributions from blades, nacelle, tower and monopile, which can be expressed by

$$\begin{aligned} E_k = \frac{1}{2}\sum_{j=1}^{3}\int_0^R \overline{m}_{b,j}\dot{u}^2_{b,j}(r)\mathrm{d}r + \frac{1}{2}M_{nac}\dot{u}^2_{nax} + \frac{1}{2}\int_{h_1}^{h_2}\overline{m}_{tow}\dot{u}^2_{tow}\mathrm{d}z \\ + \frac{1}{2}\int_0^{h_1}\overline{m}_{pile}\dot{u}^2_{pile}\mathrm{d}z \end{aligned}, \tag{9}$$

where M_{nac} is the mass of the nacelle. $\overline{m}_{bj}$, $\overline{m}_{tow}$ and $\overline{m}_{pile}$ denote the mass per unit length of blade, tower and monopile, respectively. The first term in Eq. (9) represents the kinetic energy of three blades and can be determined using the findings from Sun et al. [23].

The total potential energy of the system is given by

$$E_p = E_{p,\ b} + E_{p,\ tow}, \tag{10}$$

where, $E_{p,\ b}$ denotes the potential energy of three blades, considering contributions from blade bending, centrifugal forces, and gravitational effects [24]. The strain energy

due to shear deformation is generally negligible and is therefore ignored in this study. $E_{p,\ tow}$ represents the elastic potential energy in both the *x* and *y*-directions of the tower segment of height h_t, and is given by

$$E_{p,\ tow} = \frac{1}{2}\int_0^{h_t} EI(z)\left(\varphi_{1x}^{''}\right)^2 q_7^2 dz + \frac{1}{2}\int_0^{h_t} EI(z)\left(\varphi_{1y}^{''}\right)^2 q_8^2 dz. \quad (11)$$

The dynamic equations of the wind turbine model are derived using Lagrange's equation, which is expressed by

$$\frac{d}{dt}\left(\frac{\partial L}{\partial \dot{q}}\right) - \frac{\partial L}{\partial q} = Q, \quad (12)$$

where $L = E_k - E_p$, and Q represents the generalized non-conservative forces. This equation can be written component-wise as

$$\frac{d}{dt}\left(\frac{\partial E_k\left(t, \dot{q}_i(t), q_i(t)\right)}{\partial \dot{q}_i(t)}\right) + \frac{\partial E_p\left(t, q_i(t)\right)}{\partial q_i(t)} - \frac{\partial E_k\left(t, \dot{q}_i(t), q_i(t)\right)}{\partial q_i(t)} = Q_i(t). \quad (13)$$

where q_i and Q_i denote the components of q and Q, respectively, both being functions of time t. The subscript i ranges from 1 to 12, with detailed definitions provided in Section 2.1.

Substituting Eqs. (9–10) into Eq. (13), we obtain the matrix form of the system's dynamic behavior of OWT, which is

$$M\ddot{q} + C\dot{q} + Kq = Q_{wd} + Q_{wv} + Q_{sl}, \quad (14)$$

where M, C and K are the mass, damping and stiffness matrices of the system, each being a 12×12 matrix (see Appendix for details). Q_{wd}, Q_{wv} and Q_{sl} represent the load vectors due to wind, wave and soil, respectively. This governing dynamic equation is solved numerically using MATLAB's (MATLAB 2022b, MathWorks, The United States of America) ode45 solver, a robust Runge-Kutta-based integrator. This solver employs adaptive step-size control to balance computational efficiency and accuracy, automatically adjusting the time step based on local truncation error estimates.

2.3. Loading characteristics

2.3.1. Aerodynamic loading

The wind speed consists of both the mean wind speed and turbulent wind components. Since wind loads on OWT primarily act on the blades, the wind field across the entire swept area of a 22-MW turbine is determined using data from the TurbSim project [25], with the mean wind speed set at the rated cut-out speed of 25 m/s. **Figure 2** illustrates the wind speed distribution at the hub height and across the rotor swept area.

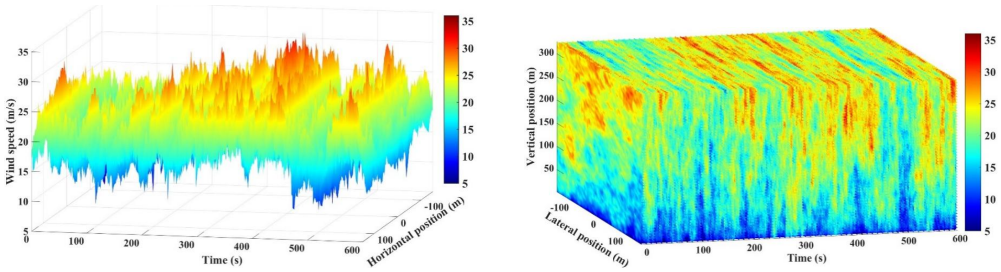

(a) **(b)**

Figure 2. Map of wind speed over time: **(a)** Wind speed distribution at the hub, and **(b)** wind speed distribution of the wind turbine.

Based on the virtual work principle and the blade element momentum (BEM) theory, the generalized forces caused by wind loads were computed. The virtual work done by aerodynamic forces can be expressed as

$$\delta W_{wind} = \sum_{j=1}^{3} \left\{ \int_0^R P_{Tj}(r,t) \left(\varphi_{2x} \delta q_j + \delta u_{nax}^x \cos\phi_j + \delta u_{nax}^z \sin\phi_j \right) dr + \int_0^R P_{Nj}(r,t) \left(\varphi_{2y} \delta q_j + \delta u_{nax}^y \right) dr \right\} . \quad (15)$$

The generalized force Q_j induced by wind load is obtained by

$$Q_j = \frac{\partial \left(\delta W_{wind} \right)}{\partial \left(\delta q_j \right)} . \quad (16)$$

By substituting Eq. (15) into Eq. (16), the generalized force components due to wind for each degree of freedom can be expressed as

$$\begin{aligned} Q_{i,wd} &= \int_0^R P_{Ti}(r,t) \varphi_{2y} dr \quad i = 1,2,3 \\ Q_{i+3,wd} &= \int_0^R P_{Ni}(r,t) \varphi_{2fa} dr \quad i = 1,2,3 \\ Q_{7,wd} = Q_{9,wd} &= \frac{1}{h_n} Q_{11,wd} = \sum_{j=1}^{3} \int_0^R P_{Nj}(r,t) dr \\ Q_{8,wd} = Q_{10,wd} &= -\frac{1}{h_n} Q_{12,wd} = \sum_{j=1}^{3} \int_0^R P_{Tj}(r,t) \cos\phi_j dr \end{aligned} . \quad (17)$$

Since wind speed varies continuously over time, the corresponding aerodynamic forces acting on the wind turbine also change dynamically. Based on Eq. (17), this study computed the time-varying generalized forces across different degrees of freedom due to wind loading over the initial 600 s, as illustrated in **Figure 3**.

2.3.2. Wave loading

In this study, the wave-induced loads on the monopile OWT are calculated using the Morison equation. The horizontal force dF_{wv} acting on a differential segment dz of the monopile due to wave action can be expressed as

$$dF_{wv} = \frac{\pi D^2}{4} C_M \rho \ddot{u} dz + \frac{\rho}{2} C_D D \dot{u} \left| \dot{u} \right| dz, \tag{18}$$

where C_M and C_D are the inertia and drag coefficients, respectively (with C_M = 1.0 and C_D = 0.6 used in this study). ρ is the water density, taken as 1025 kg/m³. D denotes the diameter of the monopile. $\ddot{u}$ and $\dot{u}$ are the wave-induced horizontal acceleration and velocity of the water particles.

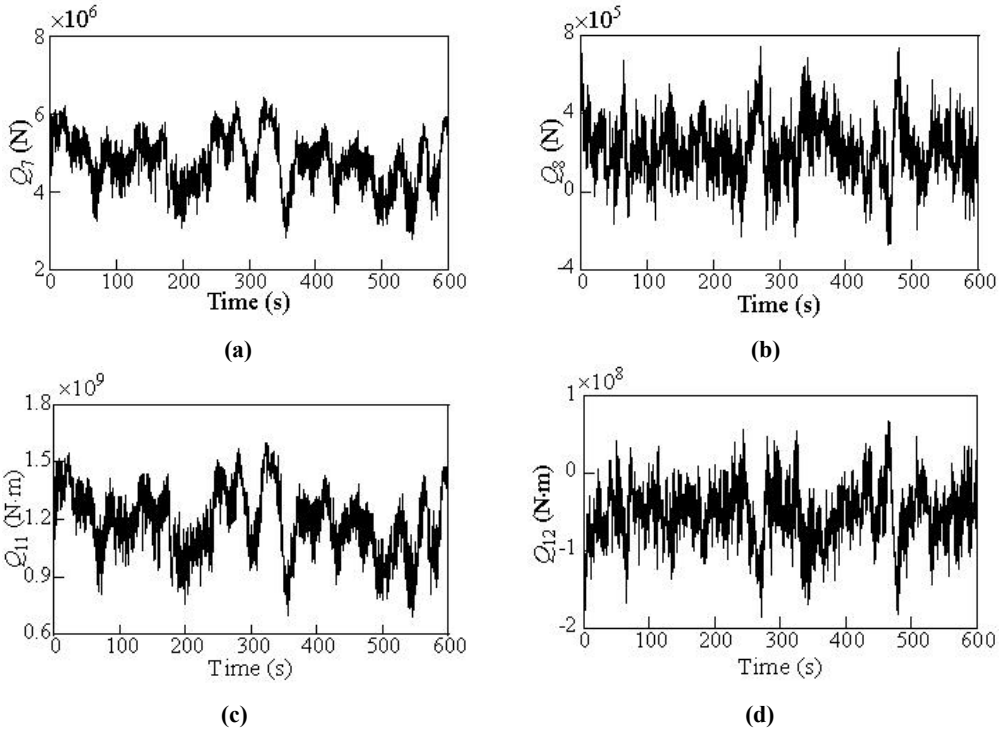

Figure 3. Generalized force caused by wind across different degrees of freedom: **(a)** $Q_{7,wd}$; **(b)** $Q_{8,wd}$; **(c)** $Q_{11,wd}$; **(d)** $Q_{12,wd}$.

A linear Airy wave model is adopted. The surface elevation $\eta(t)$ of the wave is described by:

$$\eta(t) = \frac{1}{2} H_s \cos(kx - \psi t), \tag{19}$$

where H_s, k and ψ represent the wave height (m), wave number (m^{-1}) and angular frequency (rad/s), respectively.

The velocity and acceleration of water particles under the wave are given by

$$\begin{aligned} \dot{u} &= \frac{H_s \pi \cosh\left[k\left(z + d_w\right)\right]}{T_w \sinh\left(k d_w\right)} \sin(kx - \psi t) \\ \ddot{u} &= \frac{2 H_s \pi^2 \cosh\left[k\left(z + d_w\right)\right]}{T_w^2 \sinh\left(k d_w\right)} \sin(kx - \psi t) \end{aligned}, \tag{20}$$

where T_w is the wave period, set to 12 seconds in this study, and z is the vertical coordinate measured from the still water level.

The virtual work due to the wave load is defined as

$$\delta W_{wv} = \int_{h_m}^{h_w(t)} dF_{wv} u_{pile}^x D dz, \tag{21}$$

where h_m and $h_w(t)$ represent the elevations of the mudline and the instantaneous water surface, respectively.

The generalized forces resulting from wave loading are computed as

$$\begin{aligned} Q_{j,wv} &= 0, \quad j = 1, 2, 3, \ldots, 8, 10, 12 \\ Q_{9,wv} &= \int_{h_m}^{h_w(t)} dF_{wv} dz \\ Q_{11,wv} &= \int_{h_m}^{h_w(t)} dF_{wv} z dz \end{aligned} \quad . \tag{22}$$

Figure 4 illustrates the time history of the generalized forces induced by wave loading over the first 600 seconds. Since the wave model used is a linear Airy wave, the resulting forces exhibit nearly periodic sinusoidal behavior.

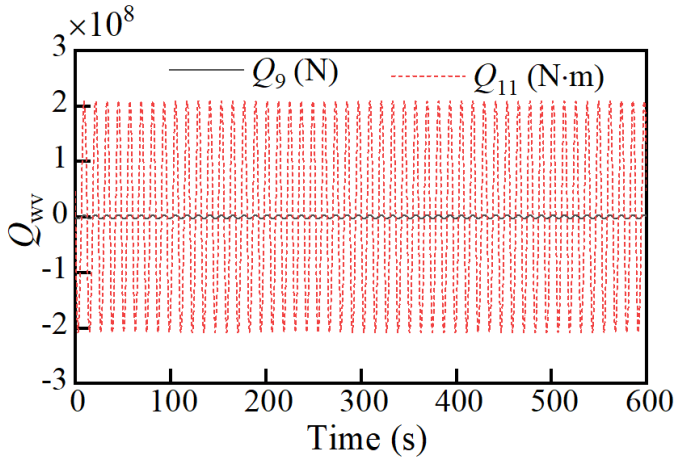

Figure 4. Generalized force caused by the wave across different degrees of freedom.

2.3.3. Soil loading

In practical offshore engineering, monopile foundations of OWT are continuously interacting with the surrounding soil due to the combined effects of wind, waves, and other environmental loads. In this study, the SPI effect is represented in terms of load response using a nonlinear $p - y$ curve, which defines the relationship between lateral soil resistance p and lateral displacement y. The $p - y$ curve for soft clay can be described as

$$p = \begin{cases} \frac{p_u}{2} \left(\frac{y}{y_c} \right)^{1/3} & y \leq 8y_c \\ p_u & y > 8y_c \end{cases}, \tag{23}$$

where p_u (N/m) represents the ultimate lateral resistance of the soil, and y_c (m) is the lateral displacement at which the soil reaches half of its ultimate resistance. p_u can be further determined by soil parameters including γ and Cu according to the Code for Pile Foundation of Harbor Engineering. γ represents the effective unit weight of soil, defined as the effective weight per unit volume. Cu denotes the undrained shear strength , quantifying the soil's shear resistance under rapid loading without drainage. The variable y essentially corresponds to the lateral displacements of the monopile in the x- and y- directions, denoted by u_{pile}^{x} and u_{pile}^{y}, respectively.

The virtual work due to soil resistance is expressed as

$$\delta W_{soil} = \int_0^{h_m} \left[p^y(z,t)\delta u^y_{pile} + p^x(z,t)\delta u^x_{pile} \right] D dz. \tag{24}$$

The generalized force due to pile-soil interaction is determined from the variation of virtual work with respect to the generalized coordinates, which is

$$Q_{j,soil} = \frac{\partial\left(\delta W_{soil}\right)}{\partial\left(\delta q_j\right)}. \tag{25}$$

By substituting Equation (24) into Equation (25), the generalized forces caused by soil can be obtained as

$$\begin{aligned} Q_{j,soil} &= 0, \quad j = 1,2,3,\ldots,8 \\ Q_{9,soil} &= D\int_0^{h_m} p^x(z,t)dz \\ Q_{10,soil} &= D\int_0^{h_m} p^y(z,t)dz \\ Q_{11,soil} &= D\int_0^{h_m} p^x(z,t)zdz \\ Q_{12,soil} &= -D\int_0^{h_m} p^y(z,t)zdz \end{aligned} . \tag{26}$$

These generalized forces are nonlinear physical quantities that depend on the lateral displacements at the base of the monopile, specifically the generalized coordinates q_9, q_{10}, q_{11} and q_{12}.

3. Results and discussion

3.1. Model description

This study performs a dynamic analysis based on the 22-MW OWT proposed by the International Electrotechnical Committee (IEC), which is a representative structure of large-scale offshore wind power systems. Detailed parameters are listed in **Table 1**. In this model, the tower and blades are modeled as elastic bodies, while the monopile foundation is assumed to be rigid due to its high stiffness. The monopile structure with an outer diameter of 10 m and a thickness ranging from 72.026 mm to 91.552 mm is applied. The tower is a non-uniform structure, with a bottom diameter of 10 m and wall thickness of 72.026 mm, reducing to a top diameter of 6 m with a wall thickness of 38.444 mm. The surrounding soil is classified as silty clay, with the effective unit weight of γ = 9.6 kN/m^3 and undrained shear strength of *Cu* = 70 kPa.

Table 1. Main parameters of 22-MW offshore wind turbine.

Parameter	Value
Rated power (MW)	22
Rotor diameter (m)	283.22
Cut-in wind speed (m/s)	3

Table 1. *Cont.*

Parameter	Value
Cut-out wind speed (m/s)	25
Rated wind speed (m/s)	10.84
Min. rotor speed (rpm)	1.975
Max. rotor speed (rpm)	7.162
Hub height (m)	170
Number of blades	3
Blade mass (t)	82.33
Nacelle mass (t)	850.70
Tower mass (t)	1574.04
Monopile mass (t)	2097.21

3.2. Dynamic analysis of OWT under cut-out wind speed

Taking a cut-out wind speed of 25 m/s as a representative case, the turbulence intensity is defined according to IEC Class A. The wave condition is modeled using a linear wave with a height of 4 m and a period of 12 s. The system's stiffness, mass and damping matrices are all 12×12 configuration due to introducing the influence of SPI effect. When the SPI effect is neglected, the translational and rotational displacements at the pile tip (denoted as q_9, q_{10}, q_{11} and q_{12}) are constrained to zero. Consequently, the system matrices for stiffness, mass and damping reduce to an 8×8 configuration, effectively decoupling the substructure dynamics from the soil domain and simplifying the analysis to a fixed-base boundary condition. The time displacement and the Fourier amplitude spectra (FAS) curves of the nacelle displacement in the *x*- and *y*- directions under combined wind, wave and soil loading are determined.

The nacelle displacements in the x-direction with and without SPI effect are compared (see **Figure 5a**). The results reveal that the turbine's large-scale structure induces measurable displacement at the monopile tip. During the initial 300 s transient phase, the nacelle displacements are smaller when SPI effect is considered. However, once the system stabilizes beyond 300 s, neglecting SPI effects leads to significant displacement overestimation. This discrepancy arises because omitting soil resistance results in exaggerated structural flexibility. FAS curves reveal that soil-pile interaction shifts the dominant frequency and reduces peak displacements by over 30%.

Figure 5b displays FAS curve of nacelle displacement in the x-direction derived from Fourier transform analysis. When the SPI effect is considered, distinct peaks corresponding to the tower and wave frequencies are observed. Soil-induced changes in effective stiffness transform a single-frequency response into multiple frequencies with reduced amplitudes. This result indicates that soil contributes both stiffness and damping, turning the system from linear to viscoelastic, which helps suppress structural vibrations.

Figure 6 presents the time- and frequency-domain responses in the y-direction. Due to smaller loads in this direction, the soil behaves almost like a fixed support, and the effect of SPI effect is minimal on structural dynamics.

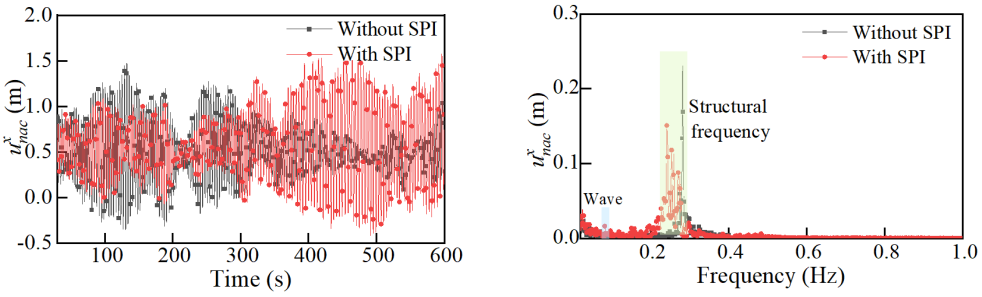

(a) **(b)**

Figure 5. Dynamic responses of wind turbine with and without SPI effect: **(a)** Time-displacement; **(b)** FAS curves of nacelle displacement in the x-direction.

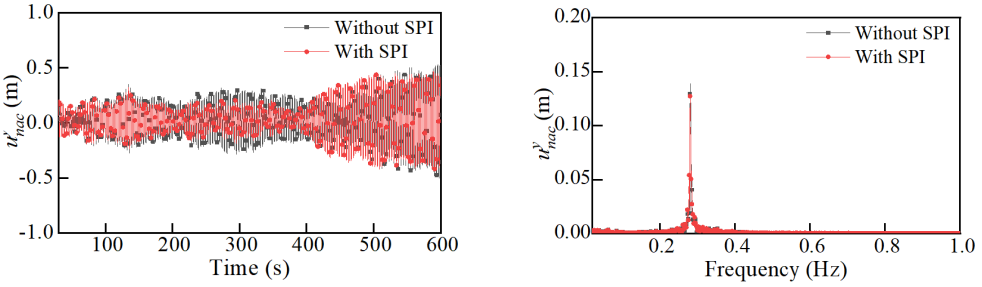

(a) **(b)**

Figure 6. Dynamic response of nacelle displacement in the y-direction for wind turbine with and without SPI effect: **(a)** time-displacement; **(b)** FAS results.

3.3. Damping effect

The $p - y$ curve primarily accounts for stiffness, providing limited damping. However, due to interparticle friction and pore fluid viscosity, soils possess inherent energy dissipation capacity. The damping ratio significantly affects the structural response of OWT under complex loads. **Table 2** summarizes the damping ratios adopted in different literature sources.

Table 2. Damping Ratio Range in different reference.

Reference	Damping Ratio Range	Key Conditions
Tarp et al. (2009) [26]	0.8%	Generalized sandy or clayey North Sea
Damgaard and Andersen (2012) [27]	0.8%–1.3%	Medium dense sand and soft clay
Shirzadeh et al. (2013) [28]	0.25%	Dense sand with layer of stiff clay
Carswell et al. (2015) [29]	0.17%–0.28%	Soft, stiff, and hard clay
Arany et al. (2016) [30]	0.444–1%	-
Zuo et al. (2018) [31]	1%	-
Bisoi and Haldar (2015, 2019) [32,33]	8%	Clay
Jindal et al. (2024) [34]	4.5%–5.9%	Silica sand

Two cases with damp ratios of 0.8% and 8% are analyzed. **Figure 7** shows the nacelle displacements in the *x*-direction when damping ratios of 0%, 0.8% and 8% is considered. As damping increases, *x*-displacements decrease (see **Figure 7a**). **Figure 7b** shows higher damping shifts the frequency to the right, consistent with its effect on equivalent stiffness. While the amplitude does not always reduce significantly due to possible multi-degree-of-freedom coupling, the damping suppresses multiple

resonances and narrows the resonance bandwidth. Additionally, increasing damping weakens wave-induced frequency responses in the spectrum. Therefore, soil stiffness and damp must be considered in dynamic analysis.

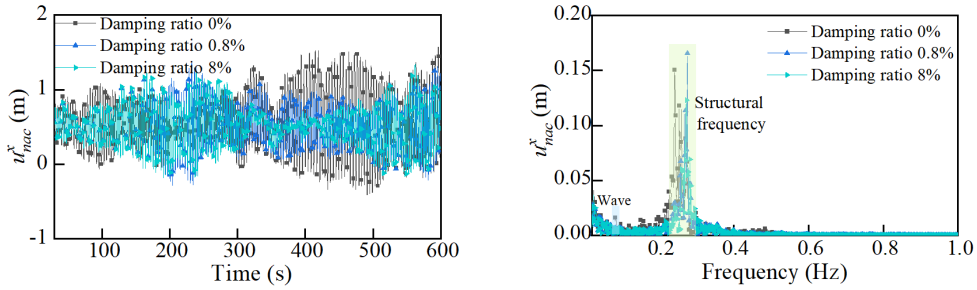

Figure 7. Dynamic responses of wind turbine under different damping ratios: **(a)** Time-displacement; **(b)** FAS curves of nacelle displacement in the x-direction.

3.4. Influence of wind speed and shear strength

In this section, a cut-in wind speed of 3 m/s is used to study the dynamic response of OWT. **Figure 8a** compares the frequency domain response of the nacelle displacement in the *x*-direction under cut-in wind speed, showing minimal differences between fixed base and soil-inclusive models, except when large damping is introduced. This confirms that soil acts effectively as a fixed support under low load conditions.

To confirm consistent dynamic behavior across soil property variations and validate the robustness of the structural control strategy, different undrained shear strength is applied. **Figure 8b** illustrates the frequency response when the soil has a lower strength with γ = 9.3 kN/m^3 and Cu = 60 kPa. These results reveal similar dynamic patterns, confirming the robustness of the conclusions under varying soil properties. When SPI effects are considered, distinct peaks emerge at the tower and wave frequencies. Soil-induced changes in effective stiffness transform the single-frequency response into multiple frequencies with reduced amplitudes, demonstrating that soil provides both stiffness and damping, turning the system from linear to viscoelastic to suppress structural vibrations.

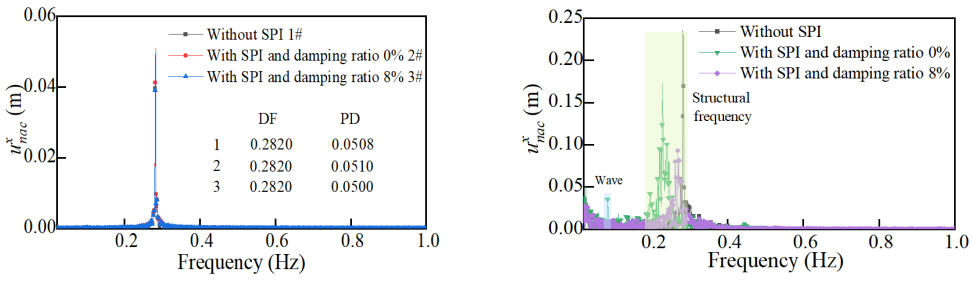

Figure 8. Dynamic response of nacelle displacement in the x-direction at the case of: **(a)** cut-in wind speed; **(b)** *Cu*=60 kPa.
Note: The key parameters of curves in **Figure 8a** include peak displacement (PD), dominant frequency (DF).

Some soil-specific $p - y$ curves for sand and stiff clay to the dynamic model are introduced to let the model work better with different soil types and simulate SPI reliably in various situations [35]. Based on the Code for Pile Foundation of Harbor

Engineering, the $p-y$ curve formula for sandy soils can be expressed as follows

$$p = \psi p'_u \tanh\left(\frac{KZ}{\psi p'_u} y\right), \tag{27}$$

where $p'_u\ (kN/m)$ is the ultimate horizontal soil resistance per unit pile length at depth Z below mudline. ψ is a parameter related to depth-diameter ratio and K is initial modulus of soil resistance (kN/m³). According to the API specifications, stiff clay is not explicitly distinguished as a separate soil category. Instead, the design approach for stiff clay adapts parameters from the soft clay $p-y$ curve model to accommodate its unique soil properties.

This study simulates the dynamic response of offshore wind turbines under cut-in and cut-out wind speed scenarios. To comprehensively characterize their behavior across multiple operational conditions, three additional wind speeds (5 m/s, 10 m/s, and 15 m/s) spanning from cut-in to cut-out regimes are analyzed. Key dynamic characteristics and FAS curves are derived, as illustrated in **Figure 9**. **Figure 9a** depicts the nacelle displacement over 600 seconds under varying wind speeds, incorporating pile-soil interaction and a damping ratio of 0.8%. The results confirm that displacement amplitude increases with wind speed. **Figure 9b** presents the corresponding FAS curves of nacelle displacement. At lower wind speeds, the spectra display simplified dominant frequency peaks. In contrast, the 25 m/s case in **Figure 5b** reveals complex multi-frequency states with sideband harmonics, indicating load-induced vibration modulation. At low external forces, damping effects are negligible due to dominantly elastic soil behavior, resulting in narrow-band Fourier peaks at structural frequencies. As external forces increase, viscous flow in saturated pores and frictional sliding between grains activate, amplifying the damping ratio.

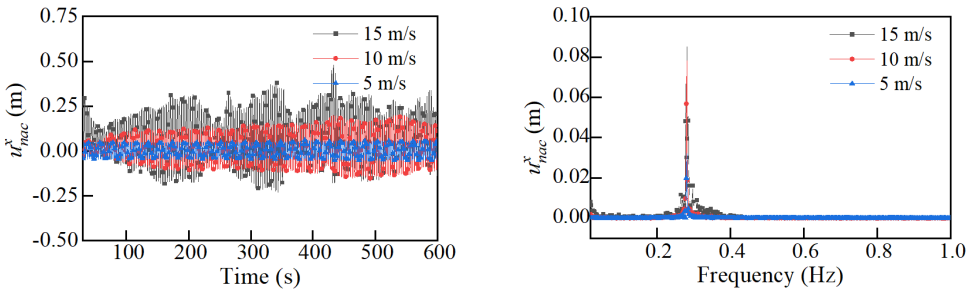

(a) **(b)**

Figure 9. Dynamic responses of wind turbine under additional wind speeds (5 m/s, 10 m/s, and 15 m/s): **(a)** Time-displacement; **(b)** FAS curves of nacelle displacement in the x-direction.

4. Conclusion

This study investigates the dynamic behavior of a monopile-supported OWT under wind-wave-soil load. A comprehensive dynamic model is developed based on Euler-Lagrange equations, incorporating rotor dynamics and SPI effect. Using the 22-MW OWT, the following conclusions are obtained. Under low external loads, such as at cut-in wind speed, modeling the pile tip as fixed or considering SPI effect yields similar dynamic behavior. However, as wind loads increase, the contribution of the SPI effect becomes more significant. Soil provides both stiffness and additional

equivalent damping, transforming the structural system from linear to viscoelastic. This significantly improves vibration suppression, highlighting the necessity of including soil-structure interaction in dynamic analyses. A consistent dynamic pattern is observed across different soil types. When only soil stiffness ($p-y$ curve) is considered, effective stiffness decreases, splitting a single resonance into several nearby, lower-amplitude frequencies. When damping is also considered, especially at low damping ratios, these multiple frequencies merge into one, reducing resonance bandwidth. The amplitude change is minimal due to potential coupling in multi-degree-of-freedom systems, but higher damping still reduces overall vibration amplitudes.

Author contributions: Conceptualization, LL; methodology, YX and HW; software, HJ; validation, LK; formal analysis, HJ; investigation, HJ; resources, LL; data curation, SW; writing—original draft preparation, YX; writing—review and editing, LL and HW; visualization, LK; supervision, HJ; project administration, JH; funding acquisition, YX. All authors have read and agreed to the published version of the manuscript.

Funding: This work was supported by the National Key Research and Development Program of China (Grants No. 2022YFB2402800).

Conflict of interest: Declare conflicts of interest or state "The authors declare no conflict of interest." Authors must identify and declare any personal circumstances or interest that may be perceived as inappropriately influencing the representation or interpretation of reported research results.

References

1. Mo R, Cao R, Liu M, et al. Effect of ground motion directionality on seismic dynamic responses of monopile offshore wind turbines. Renewable Energy. 2021; 175: 179–199. doi: 10.1016/j.renene.2021.05.036
2. Veers P, Dykes K, Lantz E, et al. Grand challenges in the science of wind energy. Science. 2019; 366(6464): eaau2027. doi: 10.1126/science.aau2027
3. Zhang J, Sui H, Ma Z, et al. Vibration damping and finite element analysis of a 10 MW jacket-type offshore wind turbine. Ocean Engineering. 2025; 331: 121236. doi: 10.1016/j.oceaneng.2025.121236
4. Igwemezie V, Mehmanparast A, Kolios A. Current trend in offshore wind energy sector and material requirements for fatigue resistance improvement in large wind turbine support structures—A review. Renewable and Sustainable Energy Reviews. 2019; 101: 181–196. doi: 10.1016/j.rser.2018.11.002
5. Yang S, Deng X, Zhang M, et al. Effect of wave spectral variability on the dynamic response of offshore wind turbine considering soil-pile-structure interaction. Ocean Engineering. 2023; 267: 113222. doi: 10.1016/j.oceaneng.2022.113222
6. Page AM, Skau KS, Jostad HP, et al. A New Foundation Model for Integrated Analyses of Monopile-based Offshore Wind Turbines. Energy Procedia. 2017; 137: 100–107. doi: 10.1016/j.egypro.2017.10.337
7. Bazeos N, Hatzigeorgiou GD, Hondros ID, et al. Static, seismic and stability analyses of a prototype wind turbine steel tower. Engineering Structures. 2002; 24(8): 1015–1025. doi: 10.1016/S0141-0296(02)00021-4
8. Asareh MA, Schonberg W, Volz J. Effects of seismic and aerodynamic load interaction on structural dynamic response of multi-megawatt utility scale horizontal axis wind turbines. Renewable Energy. 2016; 86: 49–58. doi: 10.1016/j.renene.2015.07.098
9. Sørum SH, Horn JTH, Amdahl J. Comparison of numerical response predictions for a bottom-fixed offshore wind turbine. Energy Procedia. 2017; 137: 89–99. doi: 10.1016/j.egypro.2017.10.336
10. Song M, Jiang Z, Liu K, et al. Dynamic response analysis of a monopile-supported offshore wind turbine under the combined effect of sea ice impact and wind load. Ocean Engineering. 2023; 286: 115587. doi: 10.1016/j.oceaneng.

2023.115587
11. Xi R, Yu L, Meng X, et al. Dynamic Response of a 15 MW Jacket-Supported Offshore Wind Turbine Excited by Different Loadings. Energies. 2025; 18(7): 1738. doi: 10.3390/en18071738
12. Lu Y, Xie W, Liang H, et al. Experimental and numerical study on dynamic response of offshore wind turbine subjected to earthquake loads. Ocean Engineering. 2024; 301: 117353. doi: 10.1016/j.oceaneng.2024.117353
13. Zeng F, Zhang N, Huang G, et al. Experimental study on dynamic response of a floating offshore wind turbine under various freak wave profiles. Marine Structures. 2023; 88: 103362. doi: 10.1016/j.marstruc.2022.103362
14. Sun C. Mitigation of offshore wind turbine responses under wind and wave loading: Considering soil effects and damage: Mitigation of offshore wind turbine responses under wind and wave loading: Considering soil effects and damage. Structural Control and Health Monitoring. 2018; 25(3): e2117. doi: 10.1002/stc.2117
15. Yang Y, Bashir M, Li C, et al. Mitigation of coupled wind-wave-earthquake responses of a 10 MW fixed-bottom offshore wind turbine. Renewable Energy. 2020; 157: 1171–1184. doi: 10.1016/j.renene.2020.05.077
16. Jahangiri V, Sun C. Three-dimensional vibration control of offshore floating wind turbines using multiple tuned mass dampers. Ocean Engineering. 2020; 206: 107196. doi: 10.1016/j.oceaneng.2020.107196
17. Shi S, Zhai E, Xu C, et al. Influence of Pile-Soil Interaction on Dynamic Properties and Response of Offshore Wind Turbine with Monopile Foundation in Sand Site. Applied Ocean Research. 2022; 126: 103279. doi: 10.1016/j.apor.2022.103279
18. Prowell I, Elgamal A, Lu J. Modeling the Influence of Soil Structure Interaction on the Seismic Response of a 5 MW Wind Turbine. In: Proceedings of the International Conference on Recent Advances in Geotechnical Earthquake Engineering and Soil Dynamics; 26 May 2010; San Diego, CA, USA. Available online: https://scholarsmine.mst.edu/cgi/viewcontent.cgi?article=2862&context=icrageesd
19. Abhinav KA, Saha N. Coupled hydrodynamic and geotechnical analysis of jacket offshore wind turbine. Soil Dynamics and Earthquake Engineering. 2015; 73: 66–79. doi: 10.1016/j.soildyn.2015.03.002
20. Wang T, Yu S, Wu X, et al. Lateral dynamic response of monopile offshore wind turbines in radially softened layered soil. Ocean Engineering. 2024; 299: 117289. doi: 10.1016/j.oceaneng.2024.117289
21. Akwaa GF, Gao M. Dynamic response of offshore wind turbine monopile foundation under wind-wave loads. Proceedings of the Institution of Civil Engineers - Maritime Engineering. 2023; 176(2): 48–61. doi: 10.1680/jmaen.2022.023
22. Ma H, Deng Y, Chang X. Effect of long-term lateral cyclic loading on the dynamic response and fatigue life of monopile-supported offshore wind turbines. Marine Structures. 2024; 93: 103521. doi: 10.1016/j.marstruc.2023.103521
23. Gzal M, Carrion JE, AL-Shudeifat MA, et al. Seismic mitigation of a benchmark twenty-story steel structure based on intermodal targeted energy transfer (IMTET). Engineering Structures. 2023; 283: 115868. doi: 10.1016/j.engstruct.2023.115868
24. Sun C. Semi-active control of monopile offshore wind turbines under multi-hazards. Mechanical Systems and Signal Processing. 2018; 99: 285–305. doi: 10.1016/j.ymssp.2017.06.016
25. Jonkman BJ, Buhl ML. TurbSim User's Guide. National Renewable Energy Laboratory (NREL); 2006. doi: 10.2172/891594
26. Tarp NJ, Andersen L, Christensen ED, et al. Comparing sources of damping of cross-wind motion. In: Proceedings of the European Wind Energy Conference; 14–16 September 2009; Stockholm, Sweden.
27. Damgaard M, Andersen JKF. Natural frequency and damping estimation of an offshore wind turbine structure. In: Proceedings of the Twenty-second International Offshore and Polar Engineering Conference; 17–22 June 2012; Dhodhekanisos, Greece.
28. Shirzadeh R, Devriendt C, Bidakhvidi MA, et al. Experimental and computational damping estimation of an offshore wind turbine on a monopile foundation. Journal of Wind Engineering and Industrial Aerodynamics. 2013; 120: 96–106. doi: 10.1016/j.jweia.2013.07.004
29. Carswell W, Johansson J, Løvholt F, et al. Foundation damping and the dynamics of offshore wind turbine monopiles. Renewable Energy. 2015; 80: 724–736. doi: 10.1016/j.renene.2015.02.058
30. Arany L, Bhattacharya S, Macdonald JHG, et al. Closed form solution of Eigen frequency of monopile supported offshore wind turbines in deeper waters incorporating stiffness of substructure and SSI. Soil Dynamics and Earthquake Engineering. 2016; 83: 18–32. doi: 10.1016/j.soildyn.2015.12.011
31. Zuo H, Bi K, Hao H. Dynamic analyses of operating offshore wind turbines including soil-structure interaction. Engineering Structures. 2018; 157: 42–62. doi: 10.1016/j.engstruct.2017.12.001

32. Bisoi S, Haldar S. Design of monopile supported offshore wind turbine in clay considering dynamic soil-structure-interaction. Soil Dynamics and Earthquake Engineering. 2015; 73: 103–117. doi: 10.1016/j.soildyn.2015.02.017
33. Bisoi S, Haldar S. 3D Modeling of Long-Term Dynamic Behavior of Monopile-Supported Offshore Wind Turbine in Clay. International Journal of Geomechanics. 2019; 19(7): 04019062. doi: 10.1061/(ASCE)GM.1943-5622.0001437
34. Jindal S, Rahmanli U, Aleem M, et al. Identification of soil damping for stiff piles based on experiments: soil damping curves from physical model tests. Ocean Engineering. 2024; 310: 118497. doi: 10.1016/j.oceaneng.2024.118497
35. Zhu J, Yu J, Huang M, et al. Inclusion of small-strain stiffness in monotonic p-y curves for laterally loaded piles in clay. Computers and Geotechnics. 2022; 150: 104902. doi: 10.1016/j.compgeo.2022.104902

Appendix A. System matrices and formulations for the offshore wind turbine

$$M=\begin{bmatrix}
m_{1,1} & & & & & & & & & & \\
0 & m_{1,1} & & & & & & & & & \\
0 & 0 & m_{1,1} & & & & & & & & \\
0 & 0 & 0 & m_{4,4} & & & & & & & \\
0 & 0 & 0 & 0 & m_{4,4} & & & & & & \\
0 & 0 & 0 & 0 & 0 & m_{4,4} & & & & & \\
0 & 0 & 0 & m_{7,4} & m_{7,4} & m_{7,4} & m_{7,7} & & & & \\
m_{8,1} & m_{8,2} & m_{8,3} & 0 & 0 & 0 & 0 & m_{8,8} & & & \\
0 & 0 & 0 & m_{7,4} & m_{7,4} & m_{7,4} & m_{9,7} & 0 & m_{9,\,9} & & \\
m_{8,1} & m_{8,2} & m_{8,3} & 0 & 0 & 0 & 0 & m_{10,8} & 0 & m_{9,9} & \\
0 & 0 & 0 & h_n m_{7,4} & h_n m_{7,4} & h_n m_{7,4} & m_{13,7} & 0 & m_{12,10} & 0 & m_{11,\,11} \\
-h_n m_{8,1} & -h_n m_{8,2} & -h_n m_{8,3} & 0 & 0 & 0 & 0 & m_{12,8} & 0 & -m_{12,10} & 0 & m_{12,\,12}
\end{bmatrix}$$

sym.

$m_{1,1}=\int_0^R \overline{m}_b\varphi_{2y}^2 dr$, $m_{4,4}=\int_0^R \overline{m}_b\varphi_{2x}^2 dr$

$m_{7,4}=\int_0^R \overline{m}_b\varphi_{2x} dr$, $m_{7,7}=3M_b+M_{nac}+\int_{h_1}^{h_2}\overline{m}_{tow}\varphi_{1x}^2 \mathrm{d}z$

$m_{8,1}=\cos\phi_1\int_0^R \overline{m}_b\varphi_{2y} dr$, $m_{8,2}=\cos\phi_2\int_0^R \overline{m}_b\varphi_{2y} dr$,

$m_{8,3}=\cos\phi_3\int_0^R \overline{m}_b\varphi_{2y} dr$

$m_{8,8}=3M_b+M_{nac}+\int_{h_1}^{h_2}\overline{m}_{tow}\varphi_{1y}^2 \mathrm{d}z$, $m_{9,\,9}=3M_b+M_{nac}+M_{tow}+M_{pile}$,

$m_{9,7}=3M_b+M_{nac}+\int_{h_1}^{h_2}\overline{m}_{tow}\varphi_{1x} \mathrm{d}z$,

$m_{10,8}=3M_b+M_{nac}+\int_{h_1}^{h_2}\overline{m}_{tow}\varphi_{1y} \mathrm{d}z$,

$m_{11,7}=3h_nM_b+h_nM_{nac}+\int_{h_1}^{h_2}\overline{m}_{tow}\varphi_{1x} \mathrm{z}\mathrm{d}z$,

$m_{11,11}=3h_n^2M_b+h_n^2M_{nac}+\int_{h_1}^{h_2}\overline{m}_{tow}z^2\mathrm{d}z+\int_0^{h_1}\overline{m}_{pile}z^2\mathrm{d}z$,

$m_{12,8}=3h_nM_b+h_nM_{nac}+\int_{h_1}^{h_2}\overline{m}_{tow}\varphi_{1y} \mathrm{z}\mathrm{d}z$,

$m_{12,10}=3h_nM_b+h_nM_{nac}+\int_{h_1}^{h_2}\overline{m}_{tow} \mathrm{z}\mathrm{d}z+\int_0^{h_1}\overline{m}_{pile} \mathrm{z}\mathrm{d}z$,

$m_{12,\,12}=3h_n^2M_b+h_n^2M_{nac}+\int_{h_1}^{h_2}\overline{m}_{tow}z^2\mathrm{d}z+\int_0^{h_1}\overline{m}_{pile}z^2\mathrm{d}z$,

$$K=\begin{bmatrix} k_{1,1} & 0 & 0 & 0 & 0 & 0 & 0 & 0 & 0 & 0 & 0 & 0 \\ 0 & k_{2,2} & 0 & 0 & 0 & 0 & 0 & 0 & 0 & 0 & 0 & 0 \\ 0 & 0 & k_{3,3} & 0 & 0 & 0 & 0 & 0 & 0 & 0 & 0 & 0 \\ 0 & 0 & 0 & k_{4,4} & 0 & 0 & 0 & 0 & 0 & 0 & 0 & 0 \\ 0 & 0 & 0 & 0 & k_{5,5} & 0 & 0 & 0 & 0 & 0 & 0 & 0 \\ 0 & 0 & 0 & 0 & 0 & k_{6,6} & 0 & 0 & 0 & 0 & 0 & 0 \\ 0 & 0 & 0 & 0 & 0 & 0 & k_{7,7} & 0 & 0 & 0 & 0 & 0 \\ -w^2m_{8,1} & -w^2m_{8,2} & -w^2m_{8,3} & 0 & 0 & 0 & 0 & k_{8,8} & 0 & 0 & 0 & 0 \\ 0 & 0 & 0 & 0 & 0 & 0 & 0 & 0 & 0 & 0 & 0 & 0 \\ -w^2m_{8,1} & -w^2m_{8,2} & -w^2m_{8,3} & 0 & 0 & 0 & 0 & 0 & 0 & 0 & 0 & 0 \\ 0 & 0 & 0 & 0 & 0 & 0 & 0 & 0 & 0 & 0 & 0 & 0 \\ h_nw^2m_{8,1} & h_nw^2m_{8,2} & h_nw^2m_{8,3} & 0 & 0 & 0 & 0 & 0 & 0 & 0 & 0 & 0 \end{bmatrix}$$

$$k_{1,1}=k_{b1}^{ss}+k_{b2}^{ss}-\cos\phi_1 k_{b3}^{ss}-w^2m_{1,1},\ k_{2,2}=k_{b1}^{ss}+k_{b2}^{ss}-\cos\phi_2 k_{b3}^{ss}-w^2m_{1,1}$$

$$k_{3,3}=k_{b1}^{ss}+k_{b2}^{ss}-\cos\phi_3 k_{b3}^{ss}-w^2m_{1,1},\ k_{4,4}=k_{b1}^{fa}+k_{b2}^{fa}-\cos\phi_1 k_{b3}^{fa}$$

$$k_{5,5}=k_{b1}^{fa}+k_{b2}^{fa}-\cos\phi_2 k_{b3}^{fa},\ k_{6,6}=k_{b1}^{fa}+k_{b2}^{fa}-\cos\phi_3 k_{b3}^{fa}$$

$$k_{7,7}=\int_0^{h_t} EI(z)\left(\varphi_{1x}''\right)^2 dz,\ k_{8,8}=\int_0^{h_t} EI(z)\left(\varphi_{1y}''\right)^2 dz$$

$$C=\begin{bmatrix} 0 & 0 & 0 & 0 & 0 & 0 & 0 & 0 & 0 & 0 & 0 & 0 \\ 0 & 0 & 0 & 0 & 0 & 0 & 0 & 0 & 0 & 0 & 0 & 0 \\ 0 & 0 & 0 & 0 & 0 & 0 & 0 & 0 & 0 & 0 & 0 & 0 \\ 0 & 0 & 0 & 0 & 0 & 0 & 0 & 0 & 0 & 0 & 0 & 0 \\ 0 & 0 & 0 & 0 & 0 & 0 & 0 & 0 & 0 & 0 & 0 & 0 \\ 0 & 0 & 0 & 0 & 0 & 0 & 0 & 0 & 0 & 0 & 0 & 0 \\ 0 & 0 & 0 & 0 & 0 & 0 & 0 & 0 & 0 & 0 & 0 & 0 \\ -2wm_{11,1} & -2wm_{11,2} & -2wm_{11,3} & 0 & 0 & 0 & 0 & 0 & 0 & 0 & 0 & 0 \\ 0 & 0 & 0 & 0 & 0 & 0 & 0 & 0 & 0 & 0 & 0 & 0 \\ -2wm_{11,1} & -2wm_{11,2} & -2wm_{11,3} & 0 & 0 & 0 & 0 & 0 & 0 & 0 & 0 & 0 \\ 0 & 0 & 0 & 0 & 0 & 0 & 0 & 0 & 0 & 0 & 0 & 0 \\ -2h_nwm_{11,1} & -2h_nwm_{11,2} & -2h_nwm_{11,3} & 0 & 0 & 0 & 0 & 0 & 0 & 0 & 0 & 0 \end{bmatrix}$$